Physics 108, Spring 2022

Quantum Hall effect in InAs/GaInAs heterostructure

Cameron Wagner, Gene Liu, Gayathri Ganesan, and David Saykin

(Dated: September 22, 2022)

Abstract

We demonstrated the quantum hall effect in an Indium Arsenide sample. The sample was cooled to 1.5 Kelvin and measured to fields of up to 13 Tesla. Running a 10 nA current through our sample, we measured a voltage differential between connections to the hall bar from which we worked out our hall and longitudinal resistance. We observed a quantization in our hall resistance at fields above 2T and Shubnikov–de Haas oscillations in the longitudinal direction with the longitudinal resistance dropping to 0.

CONTENTS

I. INTRODUCTION

A. Overview of QHE

Quantum Hall effect (QHE) is the effect of quantization of transversal (with respect to direction of the current flow) resistance of two–dimensional electron gas (2DEG) in the presence of the high magnetic field at low temperatures as shown in figure 3. QHE is one the greatest discoveries of the last century, which since its first observation in 1978 remains to be one of the cornerstone topics in condensed–matter physics [1, 2]. Observations of both integer and fractional QHE were distinguished with a Nobel Prize in 1985 and 1998 respectively. Measurements of QHE together with Shubnikov–de Haas oscillations are frequently used techniques which allow to unveil electronic properties of different materials. QHE is used to measure ratio of the electronic charge squared to Planck's constant e^2/h and subsequently fine structure constant. Moreover, the precision with which a resistance quantum $R_Q = h/e^2$ could be measured is so high that since 2018 CGPM uses it as a "calibration" point for now fixed values of Plank's constant and elementary charge.

Even though physicist nowadays are able to measure not only integer QHE but also fractional QHE, anomalous QHE, quantum spin Hall effect, fractional anomalous Hall effect in more and more exotic systems, building a comprehensive description of QHE proves to be a difficult challenge since the necessity to simultaneously consider effects of impurities and electron–electron interactions make the phenomenon hard to study from the theoretical standpoint [3–6]. In this paper we will confine ourselves to a simplified picture of non-interacting electrons with minimal consideration of disorder.

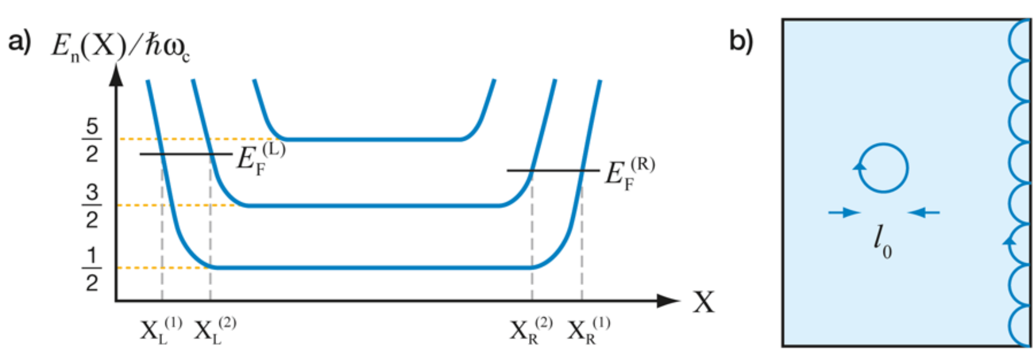

FIG. 1. Landau levels as a function of cyclotron orbits position and illustration of skipping cyclotron orbits.

B. Description of QHE

At its core quantum Hall effect could be understood within a semiclassical picture. In the presence of magnetic field B electron, driven by applied electric potential V_x, curves its trajectory under the influency of the Lorentz force $\boldsymbol{F}_L = -\frac{e}{c}[\boldsymbol{v} \times \boldsymbol{B}]$, where $e > 0$ is the elementary charge and speed of light c is present because Gaussian units are used. At high enough fields, electrons are cycling in orbits with radius $r_c = p/ecB$ called *cyclotron radius.* Similarly, to how electron in a hydrogen atom is only allowed to orbit around the nuclei in discrete orbits, at the quantum scale cyclotron orbits are also quantized. Condition of quantization could be found from the requirement that cyclotron orbit carries exactly integer number of de Brogile waves $\lambda_{dB} = h/p$, which is to equivalent to a condition of angular momentum quantization $l = pr_c \sim \hbar n$, $n \in \mathbf{N}$. From here, we deduce that energy has to be quantized $E \sim p^2/m = \hbar\omega_c n$ in the multiples of *cyclotron frequency* $\omega_c = eB/mc$. These energies are called Landau levels (LLs). Solving stationary Schrodinger equation for an electron in magnetic field confined in y direction we see that exact expression for Landau levels is $E_n\hbar\omega_c(n + \frac{1}{2})$ far from the boundaries and the energy bands curve up at the sample boundaries (see Fig. 1). Boundary states which correspond to skipping orbits transfer electrons from current source to drain without dissipation, which leads to zero longitudinal voltage drop across the sample. At the same time electrons are building up at the sample boundaries as magnetic field is increased, which leads to Hall voltage proportional to the field. However, at high field this process gets quantized, hence the Hall conductivity also becomes qunatized in units of conductivity qunatum $\sigma_Q = R_Q^{-1} = e^2/h$. Hence, at the Hall plateau conductivity σ and resistivity ρ tensors have the following form

$$\sigma = \begin{pmatrix} 0 & -R_Q^{-1}\nu \\ R_Q^{-1}\nu & 0 \end{pmatrix} \qquad \rho = \begin{pmatrix} 0 & \nu^{-1}R_Q \\ -\nu^{-1}R_Q & 0 \end{pmatrix} \qquad R_Q = \frac{h}{e^2} \approx 25.8 \text{ k}\Omega. \tag{1}$$

Here ν is the LL filling factor which is integer exactly at the plateau.

Given the observations in [7], levels about 3-8 are observable at 3-10 Tesla and a temperature of 2 Kelvin while the Shubnikov–de Haas oscillations are observable at about 0.5 Tesla and the same temperature. Both studies [8] and [7] observed that the peaks in longitudinal resistivity corresponded to magnetic field strengths were the hall voltage was rapidly varying.

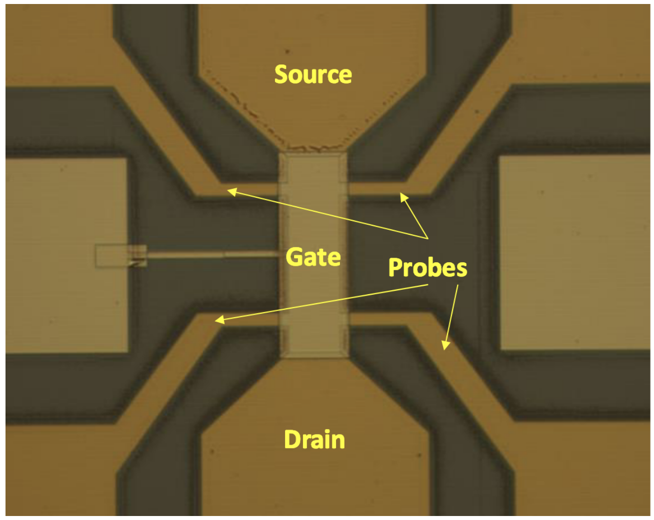

FIG. 2. Picture of our hall bar with labeled sections.

II. METHODS

To measure the quantum Hall effect, we drove a 10 nA current through our sample and measure the voltage differential between different points on the sample. Electrical connections were made to probes on the hall bar to facilitate the voltage differential measurements. This approach minimizes the contribution of the contact resistances to the measured resistance.The design of the hall bar and measurement procedure draws heavily from graphene devices in Zhang and Dean as well as the GaAs device in von Klitzing [7–9]. Our measurement procedure,

The source and drain allow for a current to through the central channel creating the flow of charge carriers necessarily for the Hall effect. For our experiment we drove an AC current at 17.76 Hz. The alternating current moves our signal away from $1/f$ noise though is also low enough so that the impedance between the contacts and the hall bar is minimal.

The probes are connected to lock-in amplifiers to measure the voltage differential between them as an analogue for resistance in the channel. These signals were amplified by a factor of 100 prior to entering the lock-in to minimize the noise from approaching the lower range of the measurement capabilities of the lock-ins. While recording data, we scanned across the range of accessible magnetic fields (from -13 Tesla to $+13$ Tesla fields) while measuring the voltage differential across one longitudinal and one hall pair of probes. The ratio of voltage differential to current through the channel gives us our resistances.

In addition, as seen in figure 1, the sample had a gate upon which a voltage differential could

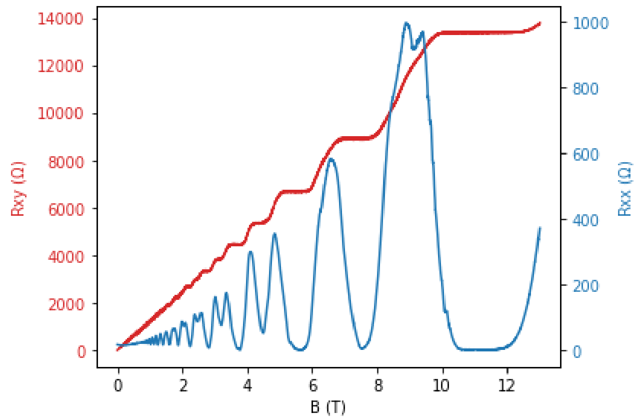

FIG. 3. A plot of our resistivity data with ρ_{xx} in blue and ρ_{xy} in red.

be applied. Much like in a capacitor, this would have the effect of changing the charge densities within the sample though through our research we left the gate grounded.

III. RESULTS

The data from the magnetic field scans is in figure 2 plotted as functions of longitudinal and hall resistivity as a function of magnetic field. Our scan of magnetic fields includes negative magnetic fields which should, in theory, include the exact same results as the positive magnetic field situation with sign flips on some terms. As such, the data shown in figure 3 and analyzed below has been symmeterized (or antisymmeterized) as appropriate to average over both directions. Looking at figure 3 on a qualitative level we see a clear quantization of allowed hall resistivity with the steps becoming larger with larger field strength. We also see that the peak in the longitudinal resistance correspond to regimes were the hall resistivity is not constant as expected.

From the data on hall resistivity, we isolated the voltage measurements during each plateau giving us a measure of the average resistivity of the plateau as well as the standard deviation to that measurement. The selection of plateaus was done manually, though small variations on parameters were attempted with no significant change in calculated resistivity of each plateau.

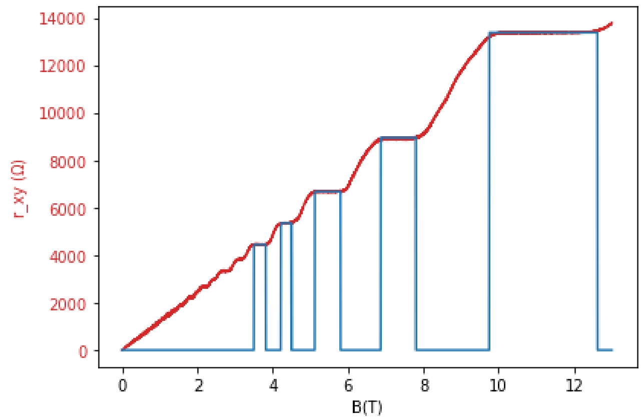

FIG. 4. A graph of hall resistivity in red with the blue highlighting our selection of the plateaus.

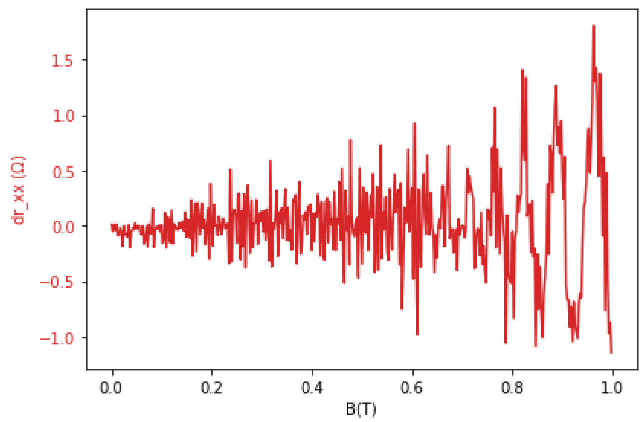

FIG. 5. A graph of ρ_{xx} at low magnetic field highlighting the first observations of SdH oscillations.

Level	Resistivity ($k\Omega$)	Reference Resistivity ($k\Omega$)
2	13.36 ($\pm$0.01)	12.91
3	8.91 ($\pm$0.03)	8.60
4	6.68 ($\pm$0.01)	6.45
5	5.35 ($\pm$0.02)	5.16
6	4.46 ($\pm$0.01)	4.30

We observe a systematic over estimation of resistivity by about 3.6%. The consistency of this error suggests that it there is an error in the measurement electronics. That said, with the given data we are unable to suggest further where this error lies. As can be seen in figure 5, SdH oscillations are first visible at slightly more than half a Tesla which matches the existing literature [7]. Lastly, our data allows us to draw conclusions about the density and mobility

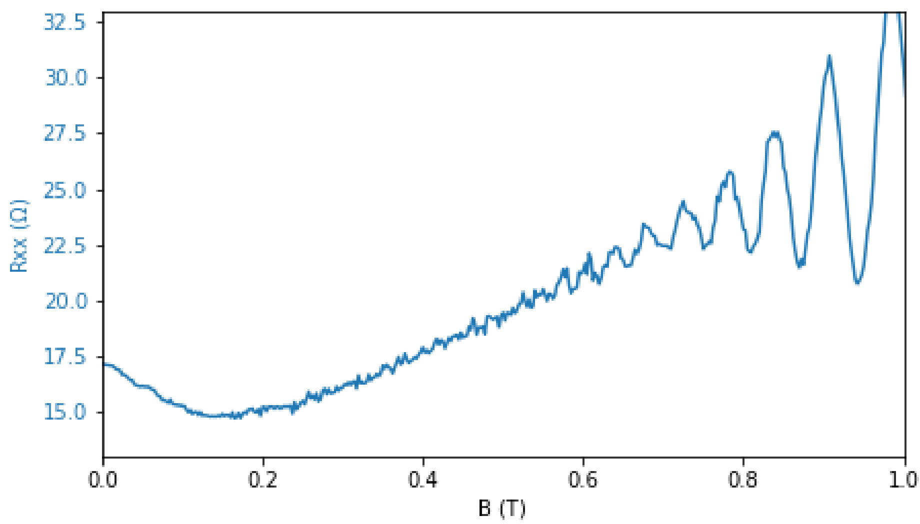

FIG. 6. Negative magneto-resistance data demonstrates weak localization behaviour.

of the carriers in our sample. From the frequency Shubnikov-de Haas (SdH) oscillations, the carrier concentration of the 2DEG can be extracted by the following formula:

$$n = \frac{e}{h}\left(\frac{1}{\Delta\frac{1}{B}}\right) \tag{2}$$

Given our data, $\Delta\frac{1}{B}$ is approximately 0.046 T^{-1} across different plateaus. Accordingly, the carrier concentration is calculated to be $5.28(\pm 0.37) * 10^{11}$ cm^{-2}, which is close with the value obtained from the low-field Hall resistance of $5.16(\pm 0.20) * 10^{11}$ cm^{-2} [10]. This carrier density also appears in calculation of carrier mobility within the sample which we find to be $3.67 \times 10^5\,\mathrm{cm}^2/\mathrm{Vs}$. This is lower than the value reported in Hsueh by a factor of about 2.5 despite our lower measured carrier density.

We now make a comment on negative magneto-resistance. Usually, materials exhibit positive magnetoresistance, since Lorentz force makes electron curve to the side making it "harder" for them to reach the current drain. It's known however, that wide class of materials including InAs/GaInAs quantum well exhibits a weak localization behaviour.

$$\sigma = \sigma_0 - \frac{e^2}{h}\ln\frac{L_\phi}{l} + \ldots, \qquad k_F l \gg 1. \tag{3}$$

Due to positive quantum interference of opposing electron trajectories scattering from impurities, the probability of return becomes larger (and conductivity becomes smaller). Such processes are possible at the scales smaller then some characteristic scale L_ϕ called *phase decoher-*

ence scale. naturally, introduction of magnetic field destroys this interference simce electron traveling forward and backward obtains different field in the presence of time-reversal breaking magnetic field. We see that at field of order 100 Gauss magnetic scale becaomes comparable to dephasing scale $l_B \sim L_\phi$. At higher fields quantum structure of Landau levels takes over and restore positive magnetoresistance.

IV. CONCLUSION

We demonstrated the quantum hall effect in an Indium Arsenide device. We observed the quantization of the hall resistivity in the high field limit and measured resistivity values with a systematic 3.6% bias above the theoretical values. We also measured carrier density and mobility finding values near those in the existing literature. Additional work is needed to isolate the cause of the discrepancy in the case of the hall resistivity. Further research should also focus on a sweep of the gate voltages to measure the impact of changing carrier densities on the measured features of the quantum hall effect.

[1] S. Wakabayashi, Jun-ichi. Kawaji, Hall effect in silicon mos inversion layers under strong magnetic fields, Journal of the Physical Society of Japan **44**, 1839 (1978).

[2] G. Klitzing, K. v. Dorda and M. Pepper, New method for high-accuracy determination of the fine-structure constant based on quantized hall resistance, Physical Review Letters **45**, 494 (1980).

[3] Y. e. a. Xie, Fractional chern insulators in magic-angle twisted bilayer graphene, arXiv arXiv:2107.10854 (2021).

[4] Y. e. a. Okazaki, Quantum anomalous hall effect with a permanent magnet defines a quantum resistance standard, Nature Physics **18**, 25 (2021).

[5] S.-C. Qi, Xiao-Liang. Zhang, The quantum spin hall effect and topological insulators, Physics Today **63**, 33 (2010).

[6] J. e. a. Klinovaja, Integer and fractional quantum anomalous hall effect in a strip of stripes model, arXiv https://doi.org/10.48550/arXiv.1412.0548 (2014).

[7] C. R. Dean, A. F. Young, I. Meric, C. Lee, L. Wang, S. Sorgenfrei, K. Watanabe, T. Taniguchi, P. Kim, K. L. Shepard, *et al.*, Boron nitride substrates for high-quality graphene electronics,

Nature nanotechnology **5**, 722 (2010).

[8] Y. Zhang, Y.-W. Tan, H. L. Stormer, and P. Kim, Experimental observation of the quantum hall effect and berry's phase in graphene, nature **438**, 201 (2005).

[9] K. v. K. N. Lecture, The quantized hall effect, Nobelprize. org (1985).

[10] C. L. Hsueh, P. Sriram, T. Wang, C. Thomas, G. Gardner, M. A. Kastner, M. J. Manfra, and D. Goldhaber-Gordon, Clean quantum point contacts in an inas quantum well grown on a lattice-mismatched inp substrate, Phys. Rev. B **105**, 195303 (2022).

[11] L. Wang, I. Meric, P. Y. Huang, Q. Gao, Y. Gao, H. Tran, T. Taniguchi, K. Watanabe, L. M. Campos, D. A. Muller, J. Guo, P. Kim, J. Hone, K. L. Shepard, and C. R. Dean, One-dimensional electrical contact to a two-dimensional material, Science **342**, 614 (2013).

Appendix A: Graphene sample preparation

1. Stacking

Different layers of our devices obtained from exfoliation (graphite back gate, HBN, graphene, HBN) were assembled using a polymer stamp by stacking them from top to bottom one at a time. During the process, several parameters including the approaching direction of the stamp to the target, the temperature of the stamp, and the approaching speed were considered to increase the success rate. One major challenge ocurrs when the target layer is attached to a much thicker layer or when a tall obstacle is nearby. Under these circumstances, the possibility of the stamp not being uniformly and fully attached to the layer increases significantly. As a result, the layer might not be picked up at all, or it might be picked up partially being teared with strain induced. To prevent this from happening, the above mentioned factors come into play. In general, the approaching speed should be slow and the direction should be chosen such that maximum area can be attached before encountering obstacles. In terms of the temperature, the stamp expands and gets stickier with higher temperature (typically 80 degree Celsius). Following these guidelines, we only failed once and were able to successfully assembled the layers to get ready for the lithography process.

2. Pattern design

The hall bar patterns were drawn using KLayout, an open source CAD software. Two samples were designed for the experiment, the first one being an eight-contact hall bar, and the second one being a ten-contact hall bar. Both of them were made of a graphite back gate and graphene encapsulated in hexagonal boron nitride (HBN). It is worth noting that for the second sample, the long axis of the hall bar is perpendicular to the interface between a monolayer and bilayer graphene. With the sample being symmetric on both sides, the intention is to study the quantum Hall effect at the interface and compare to the homogeneous case.

The hall bar pattern consists of three parts: defining the geometry of the device, making the metal 1D edge contacts, as proven to be effective[11], and depositing thicker paths as well as metal pads. In both samples, long and narrow hall bar geometries were adopted. The hall bars were symmetric in both the long and short axis so that equivalent measurements can be made. These equivalent voltage contacts were designed in case some of them fail or can be used to check sample homogeneity. In addition, several factors were taken into account to minimize errors. According to J. Volger (Note on the Hall Potential Across an Inhomogeneous Conductor), the length to width ratio of the hall bar should be larger than three to avoid the tendency of equipotential lines extending across the end and the voltage contacts. Correspondingly, the voltage contacts were made to be thin(a few nanometers), and at least one square away from the end contacts. Moreover, the edge of these contacts were designed in a zigzagged manner to improve the quality of 1D edge contacts. Following these guidelines, the geometric parameters were determined.

3. Lithography

After patterns were designed and drawn, a series of electron-beam lithography (EBL) processes were performed to fabricate the devices. The EBL processes naturally follow the three parts described in the patterning process. In the initial stage where the geometry of the hall bar is defined, a uniform layer of Polymethyl methacrylate (PMMA) is first applied using the spin coating technique. Subsequently, the sample is transferred into the JEOL JBX-6300FS Electron Beam Lithography System. In this system, a beam of high-energy electrons generated by a field emission electron source is focused by a set of electromagnetic lens. The finely-focused electron beam is then used to scan and define patterns onto the PMMA. As a positive resist, PMMA is easily washed away in regions where it is exposed using a developer, in this case a mixture of isopropanol alcohol (IPA) and water. After the development, the sample is etched using the Oxford Plasma Pro 80 Reactive Ion Etcher (RIE). This equipment is a dry-etching system utilizing high-energy ions to remove surfaces of the target materials— in this case, the regions outside the hall bar pattern as defined in the previous step. A precalculated recipe is adopted to etch through a proper depth and expose the graphite back gate. At this point, the first stage of the fabrication process is complete. The second and third stage of the processes both involve metal deposition. In a similar way, the as-prepared sample is spin-coated, exposed, and developed to define regions intended to be deposited. Next, the Kurt J. Lesker E-Beam Evaporator is used for the deposition step. During this Physical Vapor Deposition (PVD) process, the target metal (gold) is bombarded with an electron beam and is evaporated for deposition on the material to be coated with. Finally, the sample goes through a metal lift-off process by removing the PMMA so that Au is only retained in the desired contact regions. By repeating this process in

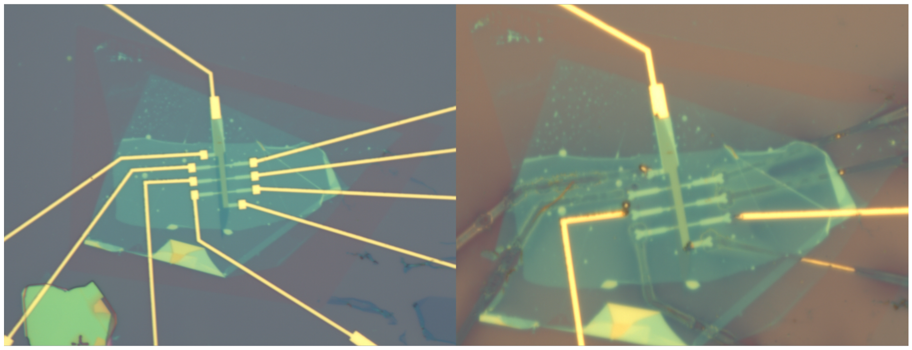

FIG. 7. On the left a sample with visible wires and on the right the same sample after an electrostatic discharge burned the wires.

the last stage with a higher beam current, thicker metal paths and larger pads are fabricated and the device fabrication is complete. Images of one of the completed devices before and after electrostatic discharge are available in figure 7.

Appendix B: Electronic noise measurements

For noise measurements, we drove a 10 nA current through a resistor with a nominal resistance of 3 $k\Omega$ test resistor. The current was generated using the voltage generator inside the lock-in amplifiers and a 100 $M\Omega$ resistor. We measured both the current through and voltage drop across the test resistor. For each lock-in we then took 120 measurements of this setup. At this resistance, the lock-ins were very consistent with a standard deviations of 0.79, 1.70, 2.14, and 1.05 Ohms. That said, they all measured a resistance under the nominal 3 $k\Omega$ which suggests that the actual resistance of the test setup was slightly smaller than the nominal value. However, the 3 lock-ins also measured different values from each other ranging from 2964 Ohms to 2979 Ohms so the discrepancy is not explained purely from the the resistor. In addition to looking at the mean and standard deviation, we plotted a histogram of the distributions of measurements in order to see any systematic bias. Looking at the data the noise is not normally distributed, but there does not seem to be a clear and obvious bias in any of the lock ins. Ideally, this procedure would have also been carried out with a 10 Ω resistor, though it was not for time considerations.

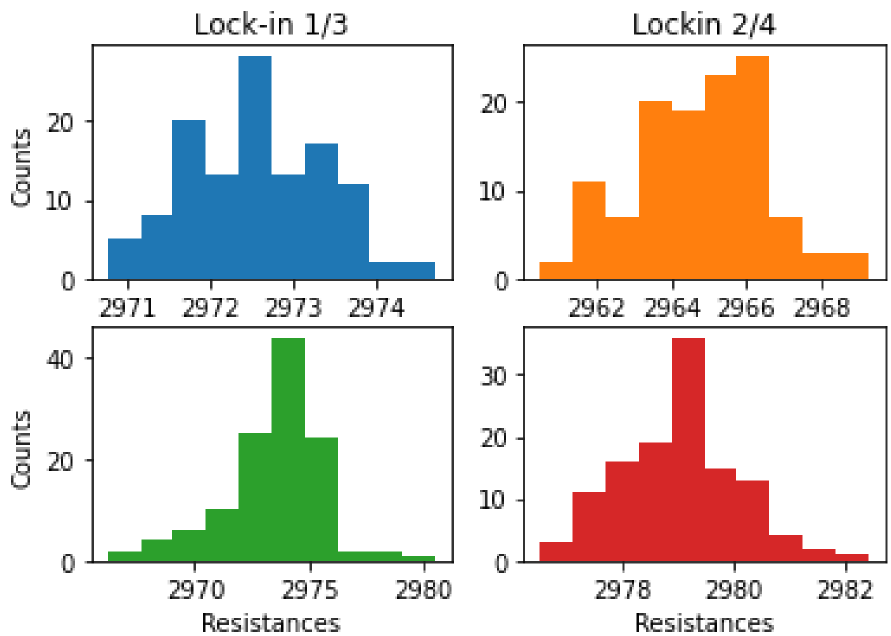

FIG. 8. Noise measurements.

Appendix C: Probe design

The probe consisted of two concentric stainless steel tubes. The outer one had an inner diameter of 7/8" and was held outside the dewar such that its bottom sat half an inch from the bottom of the magnet. The sample sat another 2 inches up inside the tube to sit at the center of the magnet. The sample was glued with PMMA to a PCB with wire bonds electrically connecting the sample to wires that ran the length of the probe. The PCB was attached to three rods by a series of nuts that were connected on the other end to a brass mounting piece which screw into the bottom of the inner tube. The brass mounting piece also had two holes that allowed wires connected to the PCB to pass through and up along inner tube. Our wires were twisted into pairs which were wrapped around the inner tube for stability. From the center of the magnet to the top of the dewar is 43.83 inches though our wires were longer to provide flexibility in probe positioning as we wired the dewar. 11 of our 12 twisted pairs used manganin wire while the 12th used copper wires specifically for the thermometer. At room temperature, the manganin wires had a resistance of about 20 Ohms while the copper wires sat at about 2.